Dynamic detection of current-induced spin-orbit magnetic fields

L. Chen [1,2,*] R. Islinger,[2] J. Stigloher,[2] M. M. Decker,[2] M. Kronseder,[2] D. Schuh,[2] D. Bougeard,[2]
D. Weiss [2] and C. H. Back [1]

[1]*Department of Physics, Technical University of Munich, Garching bei Munich, Germany*
[2]*Institute of Experimental and Applied Physics, University of Regensburg, Regensburg, Germany*

Current-induced spin-orbit torques (SOTs) in ferromagnet/nonmagnetic metal heterostructures open vast possibilities to design spintronic devices to store, process, and transmit information in a simple architecture. It is a central task to search for efficient SOT devices, and to quantify the magnitude as well as the symmetry of current-induced spin-orbit magnetic fields (SOFs). Here, we report an approach to determine the SOFs based on magnetization dynamics by means of time-resolved magneto-optic Kerr microscopy. A microwave current in a narrow Fe/GaAs (001) stripe generates an Oersted field as well as SOFs due to the reduced symmetry at the Fe/GaAs interface, and excites standing spin wave (SSW) modes because of the lateral confinement. Due to their different symmetries, the SOFs and the Oersted field generate distinctly different mode patterns. Thus, it is possible to determine the magnitude of the SOFs from an analysis of the shape of the SSW patterns. Specifically, this method, which is conceptually different from previous approaches based on line shape analysis, is phase independent and self-calibrated. It can be used to measure the current-induced SOFs in other material systems, e.g., ferromagnetic metal/nonmagnetic metal heterostructures.

I. INTRODUCTION

The investigation of the mutual conversion between charge and spin currents has witnessed significant attention in recent years due to its possible technological impact for spintronic devices [1,2]. In ferromagnet (FM)/nonmagnetic metal (NM) heterostructures, a charge current flowing in the NM along the x axis will generate a transverse spin accumulation σ along the y direction at the interface via the spin Hall effect and/or the inverse spin galvanic effect [1]. The resulting spin accumulation acts on the ferromagnetic layer via field-like (τ_{FL}) and dampinglike (τ_{DL}) spin-orbit torques (SOTs), which can be written as $\tau_{FL} = -\gamma \mu_0 h_{FL} \mathbf{m} \times \mathbf{y}$ and $\tau_{DL} = -\gamma \mu_0 h_{DL} \mathbf{m} \times \mathbf{m} \times \mathbf{y}$, where γ is the gyromagnetic ratio, μ_0 the magnetic constant, $\mathbf{m}$ the magnetization unit vector, and h_{FL} (h_{DL}) the corresponding effective fieldlike (damping-like) spin-orbit magnetic field $\mathbf{h}_{SOF}$. These torques modify the magnetization's equation of motion, i.e., the Landau-Lifshitz-Gilbert (LLG) equation, and are responsible for a number of spin-orbit related functionalities including magnetization switching [3,4], domain wall motion [5–7], and auto-oscillations of the magnetization [8,9].

II. HISTORIC DEVELOPMENT OF THE SPIN-TORQUE FERROMAGNETIC RESONANCE METHOD

To optimize material parameters leading to efficient SOTs, the magnitude of the SOFs must be determined accurately. One frequently used approach is the spin-transfer-torque

ferromagnetic resonance (STT FMR) method [10], which is based on a line shape analysis of the rectified dc voltage induced by FMR. It is generally assumed that the symmetric component of the dc voltage, V_{sym}, corresponds to the out of plane h_{DL} while the antisymmetric component, V_{a-sym}, corresponds to the in-plane Oersted field generated by the current flowing in NM. This method is so-called self-calibrated since the spin Hall angle in the NM (related to h_{DL}) is determined by the ratio of V_{sym}/V_{a-sym}. Initially, the importance of h_{FL}, which also generates V_{a-sym}, has not been properly taken into consideration. Pai *et al.* further modified this method and extracted h_{DL} and h_{FL} by measuring the dependence of V_{sym}/V_{a-sym} on the FM layer thickness t_{FM}, assuming that h_{FL} is independent of t_{FM} [11,12]. However, this does not hold since magneto-optical [13] and magnetotransport [14] methods show that h_{FL} strongly depends on t_{FM}, which possibly leads to a wrong estimation of h_{FL} and h_{DL}. A second well-established technique based on FMR is the spin-orbit-torque FMR (SOT FMR) method, which has been utilized to characterize the SOFs in single-crystalline ferromagnetic materials with broken inversion symmetry [15]. In contrast to bilayer systems, there is no in-plane Oersted field since only one layer is involved, and the single-crystalline ferromagnet acts both as spin current generator and detector (see Appendixes A and B for the differences between STT FMR and SOT FMR and details concerning these two methods). Up to now, STT FMR and SOT FMR have been used to study spin-orbit related phenomena in a large variety of materials (see the large number of references which cite Refs. [10,15]), including nonmagnetic metals [4,16], topological materials [17–20], magnetic semiconductors [21], antiferromagnets [22–24], and transition-metal dichalcogenides [25–28]. It should be noted

*lin0.chen@tum.de
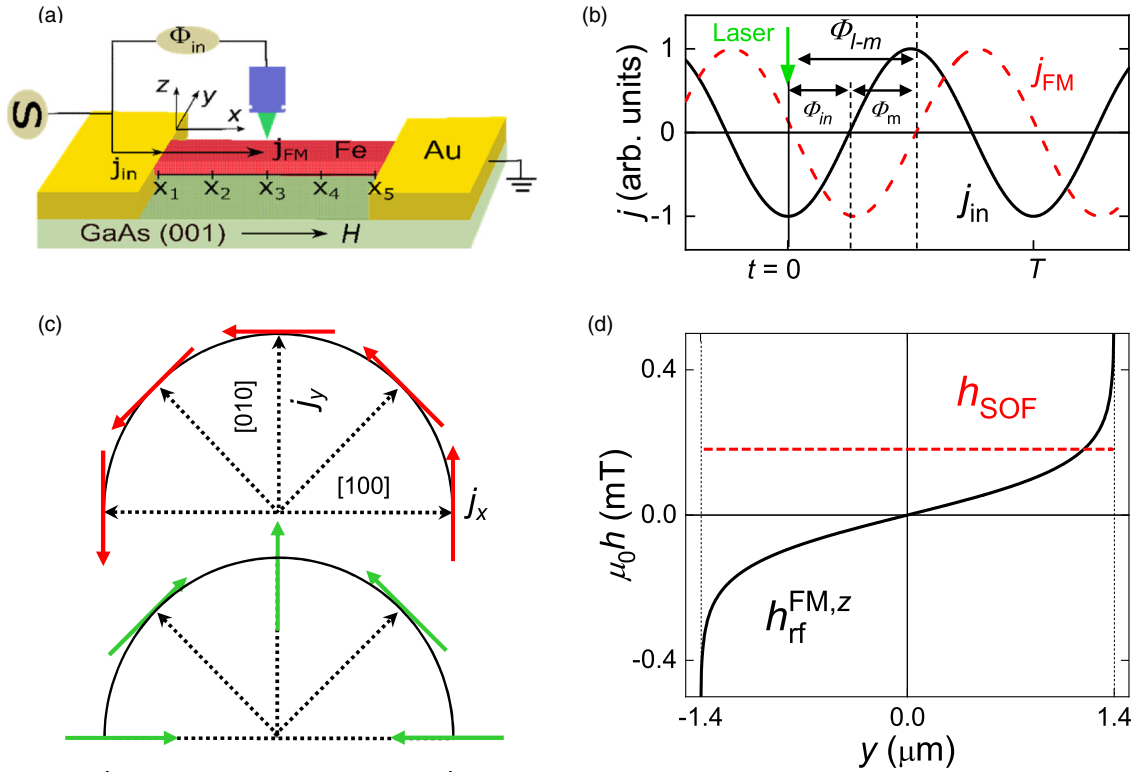
FIG. 1. Schematic of device and driving fields. (a) Schematic of the device used for the detection of magnetization dynamics driven by electric current. The out of plane component of the dynamic magnetization $m^z(t)$ is detected by time-resolved magneto-optical Kerr (TRMOKE) microscopy. A microwave current j_{FM} with a frequency f of 12 GHz is fed into the Fe stripe deposited on a semi-insulating GaAs(001) substrate, and excites $\mathbf{m}(t)$ by the combination of spin-orbit field h_{SOF} and Oersted field $h_{rf}^{FM,z}$. The external magnetic field H is applied parallel to j_{FM}. (b) Phase relations in the TRMOKE setup. Φ_{in} is the phase of input microwave current j_{in}, which can be adjusted by the time of laser pulse (green arrow). Φ_m is the assumed phase shift of j_{FM} (red dashed line). Since j_{FM} induces h_{SOF} and $h_{rf}^{FM,z}$ which drive $\mathbf{m}(t)$; thus $\mathbf{m}(t)$ is of the same phase Φ_m as j_{FM}. The phase difference between the laser pulse and $m^z(t)$, Φ_{l-m}, is thus the sum of Φ_{in} and Φ_m; i.e., $\Phi_{l-m} = \Phi_{in} + \Phi_m$. (c) Current-orientation dependence of h_{SOF} induced by Bychkov-Rashba-like (red arrow) and Dresselhaus-like (green arrow) spin-orbit interaction. Since H is parallel to j_{FM}, only the transverse components of h_{SOF} excite magnetization dynamics. (d) Lateral distributions of h_{SOF} (red dashed line) and $h_{rf}^{FM,z}$ (black solid line). h_{SOF} is symmetric across y, while $h_{rf}^{FM,z}$ is antisymmetric. The different symmetries of the excitations lead to distinctive standing spin wave patterns; i.e., the symmetric h_{SOF} excites odd spin wave modes ($n = 1, 3 \cdots$), while the antisymmetric $h_{rf}^{FM,z}$ excites even modes ($n = 2, 4 \cdots$).

that for both STT FMR and SOT FMR, the out-of-plane Oersted field $h_{rf}^{FM,z}$ generated by the current flowing in the ferromagnetic material itself contributes no net effect to the measured dc voltage since it is antisymmetrically distributed (see Appendix A). This, however, becomes the key ingredient for the present study.

For electric-current driven FMR, it is generally believed that the phase Φ_m of microwave driving current in the spin-current source materials suffers no phase shift, i.e., $\Phi_m = 0$ always holds, and Φ_m is expected to show no position dependence along the current direction of the device. Only recently, it has been noticed by spatially resolved ferromagnetic resonance phase imaging that a possible phase difference transverse to a CoFeB/Pt stripe exists [29], and affects the determination of the magnitude of h_{DL}. Note that for the sample studied in Ref. [29], a part of the microwave current flows also in the CoFeB layer, and the generated $h_{rf}^{FM,z}$ can influence the line shape and subsequently the phase. Therefore, the open questions, which have not been properly addressed so far, are as follows: Does the assumption $\Phi_m = 0$ always hold at different positions for any spin-current source material, irrespective

of the details of the material/device? If not, is it still possible to quantitatively determine SOFs by magnetization dynamics?

III. EXPERIMENTAL RESULTS

A. Evidence of phase shift for electric-current driven FMR

Here, we use Fe/GaAs (001) bilayers as a model material system to investigate a possible variation of Φ_m at different positions of the device; see Fig. 1(a). The advantages of the single-crystalline system Fe/GaAs are (i) presence of sizable interfacial SOFs having the same symmetry as FM/NM bilayers [30]; (ii) low Gilbert damping constant; (iii) the electrical current j_{FM} flows solely in Fe and thus a complex analysis can be avoided; (iv) tunable resistivity of Fe simply by changing the Fe layer thickness t_{Fe}. The measurements are carried out by phase-sensitive time-resolved magneto-optical Kerr effect (TRMOKE) microscopy [31] (see Supplemental Material [32]; also see [13,30,33]). As shown in Fig. 1(b), at certain position x, the phase difference between the pulse laser
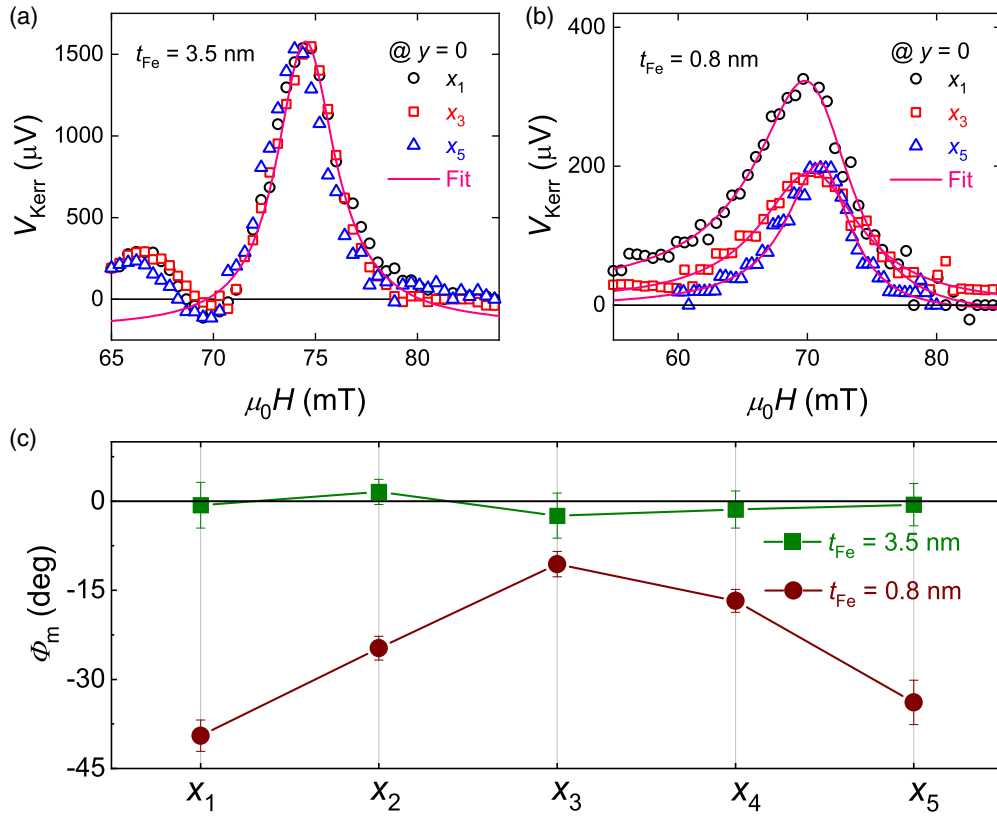
FIG. 2. Determination of the position dependence Φ_m for electric-current driven magnetization dynamics. Position-dependent Kerr voltage V_{Kerr} measured at the center of the stripe ($y = 0$, where $h_{\text{rf}}^{\text{FM},z} = 0$) for (a) Fe thickness $t_{\text{Fe}} = 3.5$ nm and (b) $t_{\text{Fe}} = 0.8$ nm. For both devices, Φ_{in} is set to 50° and the device dimensions are 6.4 μm × 100 μm. One can see that both the magnitude and the line shape for $t_{\text{Fe}} = 3.5$ nm remain unchanged, but change dramatically for $t_{\text{Fe}} = 0.8$ nm. The solid lines in (a,b) are fits to Eq. (3), which give the magnitude of φ. The bump at about 66 mT for $t_{\text{Fe}} = 3.5$ nm is due to the formation of a standing spin wave; see Sections B and C. (c) Position dependence of Φ_m obtained from Eq. (4), displaying a clear variation of Φ_m for $t_{\text{Fe}} = 0.8$ nm.

and the dynamic magnetization $\mathbf{m}(t)$, $\Phi_{l-m}(x)$, can be written as

$$\Phi_{l-m}(x) = \Phi_{\text{in}} + \Phi_m(x), \qquad (1)$$

where Φ_{in} is the controlled phase between pulse laser and input microwave current j_{in}, and $\Phi_m(x)$ the assumed x-dependent phase shift of microwave current j_{FM} in Fe. The polar Kerr signal at a certain Φ_{in} and x, $V_{\text{Kerr}}(\Phi_{\text{in}}, x)$, is proportional to the real part of the out of plane component of the dynamic magnetization m^z, which can be obtained from complex dynamic susceptibility [30]:

$$V_{\text{Kerr}}(\Phi_{\text{in}}, x) \sim \left[\text{Re}(\chi^o) h^o - \text{Im}(\chi_a^i) h^i \right] \cos \Phi_{l-m}(x)$$
$$- \left[\text{Im}(\chi^o) h^o + \text{Re}(\chi_a^i) h^i \right] \sin \Phi_{l-m}(x). \quad (2)$$

Here $\text{Re}(\chi^o)[\text{Im}(\chi^o)]$ is the real (imaginary) part of the diagonal dynamic susceptibility due to out of plane excitation h^o, and $\text{Re}(\chi_a^i)[\text{Im}(\chi_a^i)]$ is the real (imaginary) part of the off-diagonal dynamic susceptibility due to in-plane excitation h^i. For Fe/GaAs studied here, h^i contains only the position-independent h_{FL} along the y direction h_{FL}^y; i.e., $h^i = h_{\text{FL}}^y$. Note that h_{FL} along the x direction does not excite magnetization dynamics since the external magnetic field H is

applied parallel to the x axis. In contrast, h^o contains both the y-dependent Oersted field $h_{\text{rf}}^{\text{FM},z}$ and the y-independent h_{DL}; i.e., $h^o = h_{\text{rf}}^{\text{FM},z}(y) + h_{\text{DL}}$. It is worth mentioning that $\text{Im}(\chi_a^i)$ and $\text{Im}(\chi^o)$ [$\text{Re}(\chi_a^i)$ and $\text{Re}(\chi^o)$] show a symmetric (antisymmetric) line shape with respect to H, and their magnitudes can be calculated by solving the LLG equation [30].

Figures 2(a) and 2(b) show the position dependence of the Kerr voltage V_{Kerr} measured at the center of the stripe ($y = 0$ and $h_{\text{rf}}^{\text{FM},z} = 0$) under $\Phi_{\text{in}} = 50°$ for $t_{\text{Fe}} = 3.5$ and 0.8 nm. Both devices have the same dimensions of 6.4 μm × 100 μm but show an opposite temperature coefficient in the temperature dependence of the resistivity (see Appendix C). For $t_{\text{Fe}} = 3.5$ nm, the line shape as well as the magnitude of V_{Kerr} remain the same along the stripe from x_1 to x_5, while they change dramatically for $t_{\text{Fe}} = 0.8$ nm. To extract Φ_m, the characteristic V_{Kerr} spectra can be fitted by

$$V_{\text{Kerr}} = A \frac{\cos\varphi \Delta H^2 + \sin\varphi \Delta H (H - H_R)}{4(H - H_R)^2 + \Delta H^2}. \quad (3)$$

Here A is an apparatus-dependent coefficient, H_R the magnetic field at FMR, ΔH the full width at half maximum, and φ is the phase factor which determines the line shape of $V_{\text{Kerr}}(H)$.

From Eqs. (1)–(3), the magnitude of Φ_m can be derived as

$$\Phi_m = \tan^{-1} \frac{\text{Re}(\chi^o)h_{\text{DL}}\cos\varphi + \text{Im}(\chi_a^i)h_{\text{FL}}^y\sin\varphi}{\text{Re}(\chi_a^i)h_{\text{FL}}^y\cos\varphi - \text{Im}(\chi^o)h_{\text{DL}}\sin\varphi} - \Phi_{\text{in}}, \quad (4)$$

which provides a measure of the phase shift of the driving microwave current in the spin-current source material via time-resolved magneto-optical Kerr (TRMOKE) spectra. Using the corresponding dynamic susceptibilities as well as φ values for both devices, and considering that $h_{\text{DL}} \sim h_{\text{FL}}^y$, the magnitude of Φ_m can be obtained from Eq. (4). Figure 2(c) summarizes Φ_m as a function of position for both devices. One can see that Φ_m shows no significant change within experimental error for $t_{\text{Fe}} = 3.5$ nm. However, a sizable variation of Φ_m is observed for $t_{\text{Fe}} = 0.8$ nm. The variation of Φ_m could be due to the fact that the rf characteristics of Fe change from a good conductor to a dielectric upon decreasing t_{Fe} (see Appendix C). Besides ultrathin Fe, we show in the Supplemental Material [32] that sizable phase variation is also found in Py/Bi$_2$Se$_3$ bilayers, where a more resistive Bi$_2$Se$_3$ also changes the phase of microwave current. The phase variation at certain positions will not influence the line shape of the rectified dc voltage induced by the coupling of the microwave current and magnetization dynamics (Appendix B). However, the spatial variation of Φ_m could lead to the formation of a spin wave spin current traveling along the x direction [34] and subsequent conversion to a symmetric dc voltage through the spin galvanic effect if a Dresselhaus-type spin-orbit interaction is present [15,21,28]. We propose that this should be carefully examined and possibly excluded if the line shape analysis method is used to quantify the SOFs.

Therefore, it is of vital importance to establish a phase-independent technique to reliably determine the SOFs based on magnetization dynamics. Here, we report a self-calibrated and phase-independent approach to measure current-induced SOFs by analyzing the shape of the standing spin wave (SSW) mode patterns, i.e., a method which is distinctly different from previous electrical methods based on line shape analysis.

B. Formation of standing spin waves in a laterally confined Fe/GaAs stripe

Formation of SSWs is a prerequisite for this work. Figure 3(a) shows the calculated SSW eigenmodes for a 2.8 μm wide, 3.5 nm thick Fe stripe with H applied along the [110] direction of the GaAs substrate, which corresponds to the Damon-Eshbach geometry [35,36]. In the calculation, the following parameters determined by separate magnetization and FMR measurements are used: saturation magnetization $\mu_0 M_S = 2.1$ T, effective demagnetization field $\mu_0 H_K = 1.75$ T, and Landé g factor $g = 2.12$. The intersection at a frequency f of 12 GHz specifies H_R of each mode, which is expected to be observed in the experiment. The lateral confinement leads to a mode separation of 4 mT (i.e., 8 mT between odd modes), which is comparable to the magnitude of ΔH. The normalized profiles of m^z for the first five modes ($n = 1-5$), i.e., m^z as a function of space coordinate y, are displayed in Fig. 3(b). One can see that the odd (even)
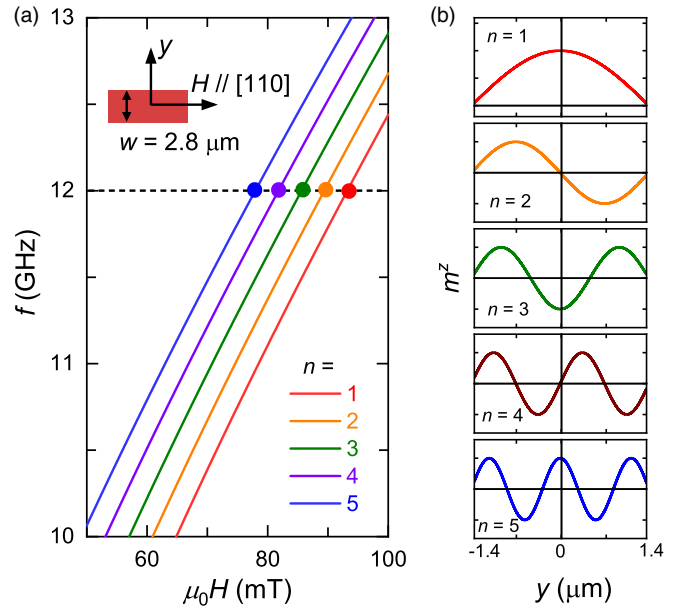
FIG. 3. Eigenmodes and distribution of confined SSWs. (a) Calculated eigenmodes for a laterally confined Fe/GaAs stripe with $t_{\text{Fe}} = 3.5$ nm and $w = 2.8\ \mu$m. The external magnetic field H is applied along the [110] direction of GaAs, and the intersection defines the required H_R for each standing spin wave (SSW) mode at $f = 12$ GHz. (b) The lateral distribution of SSW modes for $n = 1-5$. The symmetric modes ($n = 1, 3,$ and 5) can be excited by symmetric excitations; antisymmetric modes ($n = 2$ and 4) can be excited by antisymmetric excitations.

modes are symmetrically (antisymmetrically) distributed with respect to the center of the stripe. Consequently, the odd (even) modes can be excited by symmetrically (antisymmetrically) distributed driving fields due to symmetry reasons [35,36].

We first analyze the eigenmodes of the Fe/GaAs stripe under homogeneous (symmetric) excitation. The stripe, which is 2.8 μm in width and 20 μm in length with the long side along the [110] direction of the GaAs substrate, is integrated in the gap of a coplanar waveguide (CPW) by using electron-beam lithography, as shown in the inset of Fig. 4(a). Here, the Fe stripe is exposed to homogeneous excitation by an out of plane Oersted field $h_{\text{rf}}^{\text{CPW},z}$, which is generated by microwave current flowing in the signal and ground line of the CPW. According to Eq. (2), the detected Kerr signal can be simplified as $V_{\text{Kerr}}(\Phi_{\text{in}}) \sim \text{Re}(\chi^o)h_{\text{rf}}^{\text{CPW},z}\cos(\Phi_{\text{in}}+\Phi_m) - \text{Im}(\chi^o)h_{\text{rf}}^{\text{CPW},z}\sin(\Phi_{\text{in}} + \Phi_m)$. Figure 4(a) shows the normalized $V_{\text{Kerr}}(H, y)$ image measured at $\Phi_{\text{in}} = 90°$. As expected, only the odd modes with $n = 1, 3,$ and 5 appear. Figure 4(b) presents the micromagnetic simulation [33] of the SSW modes using the same parameters as those used in Fig. 3, which reproduces the experimental results well (see Supplemental Material [32]). To have a closer look at the obtained modes, we perform a horizontal scan for the data in Fig. 4(a), i.e., by placing the laser at the center of the stripe and sweeping H. As shown in Fig. 4(c), the cut shows only symmetric line shapes, which can be fitted using the corresponding cut of the simulation data in Fig. 4(b). The locations of the first, third, and fifth modes are marked by solid points, and the
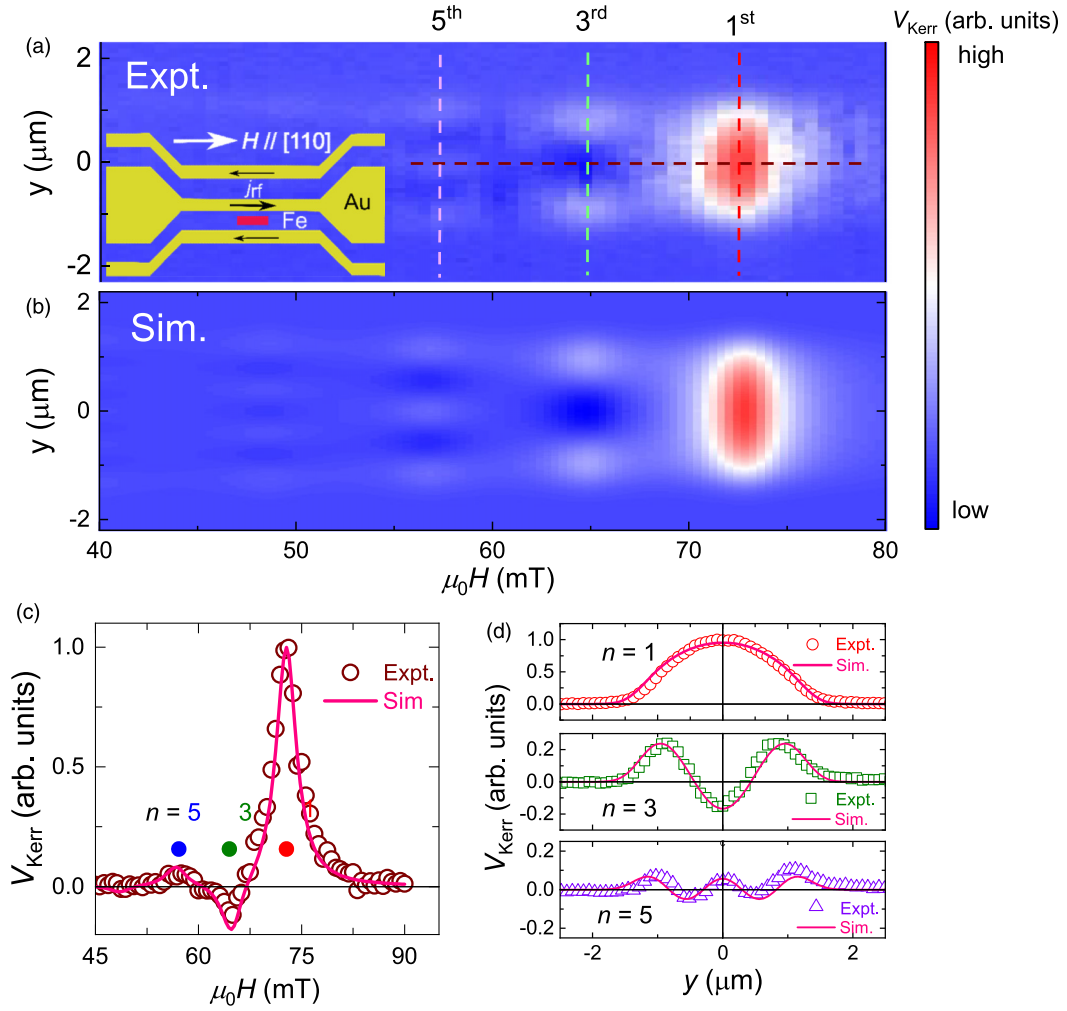
FIG. 4. SSWs driven by a symmetric excitation. (a) SSWs detected in a Fe (3.5 nm)/GaAs stripe by TRMOKE microscopy, where the magnetization dynamics is excited by a homogeneous (symmetric) out of plane Oersted field through a coplanar waveguide (CPW). Only symmetric odd modes ($n = 1$, 3, and 5) can be observed. The inset shows the schematic of the CPW device, where the Fe stripe is integrated into the gap of the CPW, and H is applied along the long axis of the stripe, i.e., along the [110] direction of GaAs. (b) Micromagnetic simulation of the SSW modes using MUMAX3, which reproduces the experimentally observed modes well. In the simulation, we use the same material parameters as for the calculation of the eigenmode and we convolve the simulation with a Gaussian beam profile. (c) Horizontal line cut of the Kerr signal at the center of the stripe ($y = 0$). The three peaks can be fitted by symmetric Lorentzians, and the positions of the first, third, and fifth modes are indicated by red, green, and blue circles, respectively. (d) Vertical cut of modes for $n = 1$, 3, and 5. All the modes show symmetric profiles and can be well fitted by MUMAX simulations.

mode spacing coincides well with the eigenmode calculation shown in Fig. 3(a). Note that the mode position differs between Figs. 3(a) and 4(c); this is because the in-plane biaxial and uniaxial magnetic anisotropies are not included in the eigenmode calculation. Since only purely symmetric line shapes are observed, one can infer that $\Phi_m = 0°$. Otherwise an antisymmetric component in the V_{Kerr} trace originating from Re(χ^o) is expected. This is not surprising since the microwave current and $h_{rf}^{CPW,z}$ are intrinsically in phase due to the fact that the CPW is impedance matched with the rf network. These results also prove the validity of the proposed phase analysis presented above. Figure 4(d) shows the first, third, and fifth modes as a function of lateral space coordinate y. All the modes show symmetric profiles with the peak wave-amplitude ratio of ∼10:2:1, which can also be well fitted by micromagnetic simulations.

C. Determination of SOFs by the shape of the standing spin wave pattern

Next, measurements are performed on a 2.8 μm wide, 100 μm long stripe orientated along the [110] direction of GaAs using an electric-current excitation as shown in Fig. 1(a). A rf-current density $j_{FM} = 1.0 \times 10^{11}$ A m^{-2} is applied to the device, and H is set parallel to j_{FM}. The magnitude of j_{FM} is calibrated by the Joule heating induced resistance increase [15]. As shown in Fig. 1(d), the driving fields here contain both symmetric h_{SOF} and antisymmetric $h_{rf}^{FM,z}$ components. In addition to the odd modes driven by the symmetric SOFs, even modes excited by the antisymmetric $h_{rf}^{FM,z}$ are expected. Figure 5(a) shows the SSW pattern measured at $\Phi_{in} = 90°$. In contrast to Fig. 4(a) where only the symmetric odd modes are observed, for the case of electric-current excitation,
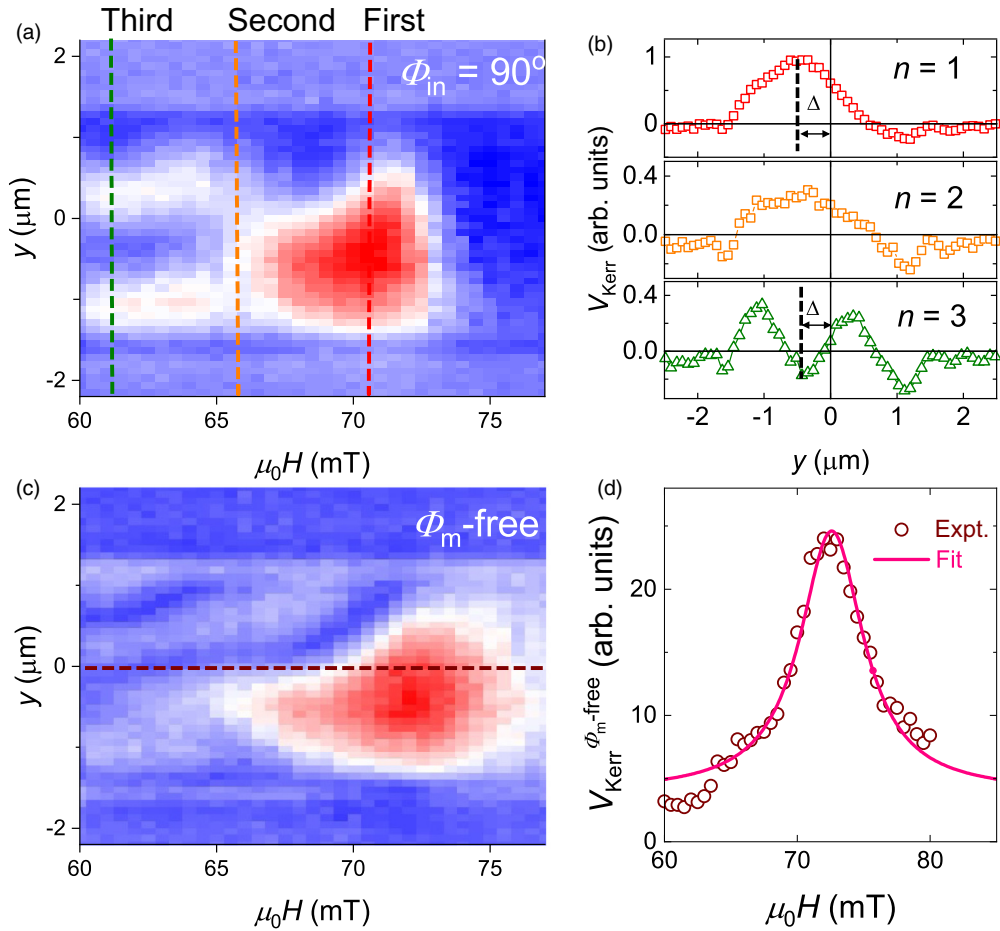
FIG. 5. SSWs driven by electric current for $t_{Fe} = 3.5$ nm. (a) Image of the TRMOKE signal measured at $\Phi_{in} = 90°$ and $j_{FM} \parallel \mathbf{H} \parallel$ [110]. (b) Profiles of the first three modes, i.e., vertical cuts along the dashed lines in (a). The position of the maxima (minima) of $n = 1$ ($n = 3$) shifts away from the center of the stripe by $\Delta \sim 0.4$ μm due to the interference with the second mode, as indicated by the dashed lines. (c) Corresponding image of $V_{Kerr}^{\Phi_m-free}$ for a [110] device obtained by square and root operation of $V_{Kerr}(0°)$ and $V_{Kerr}(90°)$; i.e., $V_{Kerr}^{\Phi_m-free} = \sqrt{[V_{Kerr}(0°)]^2 + [V_{Kerr}(90°)]^2}$. (d) Horizontal cut of $V_{Kerr}^{\Phi_m-free}$ at $y = 0$, which can be fitted by a symmetric Lorentzian.

both the first and third modes are not located at the center of the stripe anymore. This indicates the emergence of the antisymmetric second mode. Because the mode spacing is of the same magnitude as the FMR linewidth, the nearest modes merge, and the shape of the SSW pattern is dramatically altered and shifted. For example, the second mode increases V_{Kerr} of the first mode on the lower part of the stripe while reducing it on the upper side. A clearer shift of the patterns can be seen from the profile (vertical cut) of each mode. As

shown in Fig. 5(b), the maximum (minimum) position of the first (third) mode shifts away from center to the lower part of stripe by an absolute value of $\Delta \sim 0.4$ μm.

If the phase term Φ_m is unknown, it is impossible to extract the magnitude of SOF from Fig. 5(a). However, it is possible to eliminate Φ_m through square and root operations of $V_{Kerr}(\Phi_{in})$ measured at two phases with 90° phase shift. Based on Eq. (2), the Φ_m-independent Kerr voltage $V_{Kerr}^{\Phi_m-free}$ can be obtained as

$$V_{Kerr}^{\Phi_m-free} = \sqrt{[V_{Kerr}(\Phi_{in})]^2 + [V_{Kerr}(\Phi_{in}+90°)]^2},$$

$$\sim \text{Im}(\chi_a^i) h_{FL}^y \sqrt{\left[1 - \frac{\text{Re}(\chi^o)}{\text{Im}(\chi_a^i)} \frac{h_{DL} + h_{rf}^{FM,z}}{h_{FL}^y}\right]^2 + \left[\frac{\text{Re}(\chi_a^i)}{\text{Im}(\chi_a^i)} + \frac{\text{Im}(\chi^o)}{\text{Im}(\chi_a^i)} \frac{h_{DL} + h_{rf}^{FM,z}}{h_{FL}^y}\right]^2}. \tag{5}$$

The corresponding $V_{Kerr}^{\Phi_m-free}$ image for the [110]-oriented device is shown in Fig. 5(c). For the present sample with $\mu_0 H_K$ of 1.75 T, the magnitude of the susceptibility under out of plane excitation is much smaller than the in-plane one, and the ratios of the dynamic susceptibilities under the square root are determined as [30] $\text{Re}(\chi^o)/\text{Im}(\chi_a^i) = 0.1$, $\text{Re}(\chi_a^i)/\text{Im}(\chi_a^i) = -0.5$, and
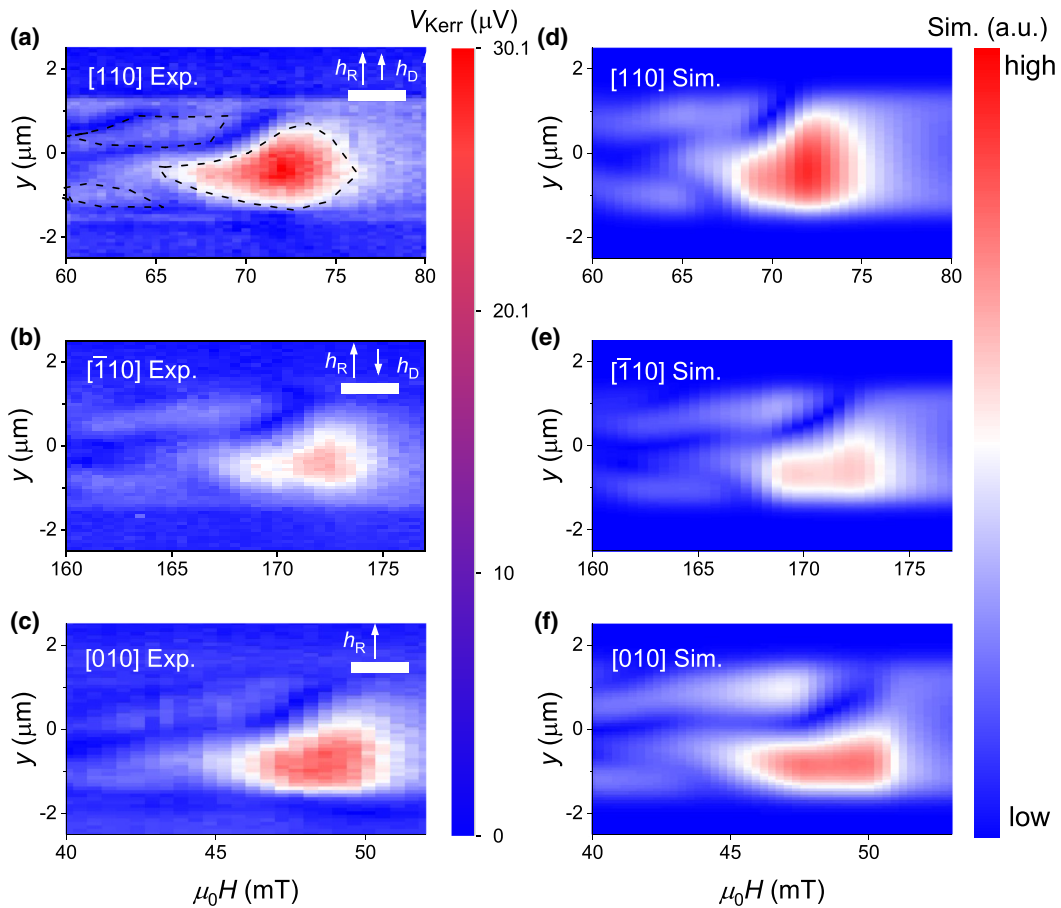
FIG. 6. Determination of SOF by the shape of SSW pattern for $t_{Fe} = 3.5$ nm. Image of $V_{Kerr}^{\Phi_m\text{-free}}(H, y)$ signal for **a** $j_{FM} \parallel \mathbf{H} \parallel [110]$, (b) $j_{FM} \parallel \mathbf{H} \parallel [\bar{1}10]$ and (c) $j_{FM} \parallel \mathbf{H} \parallel [010]$. In the plots, j_{FM} has been normalized to 1×10^{11} A m^{-2}. The configurations of the SOFs induced by Bychkov-Rashba-like h_R and Dresselhaus-like h_D are also presented in the insets. h_R and h_D are constructive for [110]-oriented devices, but destructive for [$\bar{1}$10]-oriented devices. For [010] orientation, only h_R is detected. Corresponding images obtained by micromagnetic simulations for devices oriented along (d) [110], (e) [$\bar{1}$10], and (f) [010].

Im$(\chi^o)/$Im$(\chi_a^i) = -0.2$. At the center of the stripe ($h_{rf}^{FM,z} = 0$ and $h_{DL} = h_{FL}^y$), Eq. (5) can be further simplified to

$$V_{Kerr}^{\Phi_m\text{-free}} \approx \text{Im}(\chi_a^i)h_{FL}^y \sqrt{1 + \left[\frac{\text{Re}(\chi^o)}{\text{Im}(\chi_a^i)}\right]^2 + 2\left[\frac{\text{Re}(\chi_a^i)}{\text{Im}(\chi_a^i)}\frac{\text{Im}(\chi^o)}{\text{Im}(\chi_a^i)} - \frac{\text{Re}(\chi^o)}{\text{Im}(\chi_a^i)}\right]\frac{h_{DL}}{h_{FL}^y}} = \text{Im}(\chi_a^i)h_{FL}^y \sqrt{1 + \left[\frac{\text{Re}(\chi^o)}{\text{Im}(\chi_a^i)}\right]^2}.$$

This means only h_{FL}^y contributes to $V_{Kerr}^{\Phi_m\text{-free}}$, and the effect of h_{DL} can be neglected in the analysis due to the large effective demagnetization field. Equation (5) also suggests that, at the center of the stripe, the line shape of the $V_{Kerr}^{\Phi_m\text{-free}}$ trace is symmetric with respect to H, which is confirmed by the horizontal cut shown in Fig. 5(d). However, when the laser is moved away from the center of the stripe, the above assumption becomes invalid, since $h_{rf}^{FM,z} > h_{FL}^y$ holds. The appearance of even modes excited by $h_{rf}^{FM,z}$ can alter the shape of the odd mode pattern, which, therefore, provides a phase-independent way to determine the magnitude of h_{FL}^y.

Figures 6(a)–6(c) present the images of $V_{Kerr}^{\Phi_m\text{-free}}(H, y)$ for devices structured along the [110], [$\bar{1}$10], and [010] orientations. To compare the amplitudes of $V_{Kerr}^{\Phi_m\text{-free}}$, all images

are normalized to the current density $j_{FM} = 1 \times 10^{11}$ A m^{-2}. As shown in the images, the coalescence of the first three mode patterns leads to the formation of three main regions as indicated by the closed dashed lines. The odd and even modes merge and become indistinguishable after the treatment of square and root operations. All the $V_{Kerr}^{\Phi_m\text{-free}}(H, y)$ images show similar patterns indicating similar excitations for each device. However, the maximum intensity of the Kerr signal, V_{max}, differs significantly for different crystallographic directions with $V_{max}^{[110]} = 1.2 V_{max}^{[010]} = 1.7 V_{max}^{[\bar{1}10]}$. This implies a dependence of h_{FL}^y on the current direction due to interference of Bychkov-Rashba-like and Dresselhaus-like spin-orbit interactions. As sketched in the insets of Figs. 6(a)–6(c), constructively aligned Dresselhaus h_D and Bychkov-Rashba h_R SOFs are detected ($h_{FL}^y = h_R + h_D$ for the [110] orientation,

while for the $[\bar{1}10]$ orientation, h_D and h_R add destructively ($h_{FL}^y = h_R - h_D$). For the $[010]$ orientation only h_R can be detected ($h_{FL}^y = h_R$). To quantify h_D and h_R, we repeat the micromagnetic simulations, similar to the case where the magnetization dynamics is only driven by a homogeneous $h_{rf}^{CPW,z}$ originating from the CPW, but now including both y-independent h_{FL}^y and y-dependent $h_{rf}^{FM,z}$ calculated from the Biot-Savart law. A least square algorithm is carried out to minimize the difference between images obtained by experiment and simulations (see Supplemental Material [32]). As shown by Figs. 6(d)–6(f), the corresponding simulation images reproduce the experiments reasonably well. For the [110] device, the magnitude of the extracted SOF is $\mu_0 h_R + \mu_0 h_D = 0.28$ mT; and for the $[\bar{1}10]$ device, $\mu_0 h_R - \mu_0 h_D = 0.13$ mT, which gives $\mu_0 h_R = 0.21$ mT and $\mu_0 h_D = 0.07$ mT. The magnitude $\mu_0 h_R$ in turn is consistent with the value determined from a [010] device with $\mu_0 h_R = 0.22$ mT. Moreover, we compare the magnitude of SOF obtained by SSW and dc voltage detection for the same device of $t_{Fe} = 3.5$ nm in the Supplemental Material [32], and the results show quantitative agreement between our method and dc voltage detection for samples with no phase variation. All these results indicate the validity of our method.

Although the present experiment only determines the magnitude of the fieldlike torque (corresponding to h_{FL}^y) due to the relatively large H_K value, we propose in the Supplemental Material [32] that it is also possible to determine the magnitude of fieldlike and dampinglike torques in FM/NM bilayers with a reduced H_K, showing the completeness of this method. It should be noted that to perform the SSW pattern method in FM/NM bilayers, the prerequisite is that the effective damping constant of the FM should be low (~ 0.005), which leads to sizable mode spacing comparable to the FMR linewidth. This, however, is not the case for most FM/NM bilayers [also for $t_{Fe} = 0.8$ nm shown in Fig. 2(a)] due to the large effective damping caused by extrinsic effects, such as spin pumping and/or inhomogeneous broadening. A possible solution for this problem could be using metallic ferromagnets with ultralow damping, such as CoFe [37].

IV. CONCLUSIONS

We have demonstrated by TRMOKE measurements that a possible phase variation of the driving microwave current can be detected when using electric-current excitation. We have proposed a phase-independent and self-calibrated way to quantify the spin-orbit fields by using the shift of standing spin wave patterns excited by the combined action of current-induced spin-orbit fields and Oersted field. This unique approach goes beyond the standard electrical measurements based on line shape analysis and solves a long-standing problem in the determination of SOFs based on magnetization dynamics. Our method is not specific to Fe/GaAs, but can also be used for other systems, e.g., ferromagnetic metal/nonmagnetic metal bilayers.
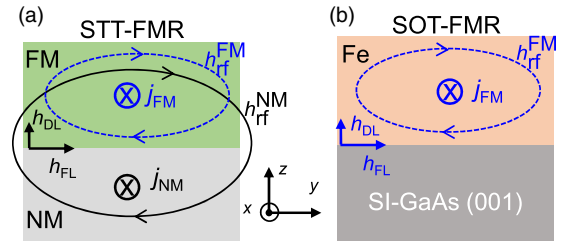
FIG. 7. Schematics of the driving fields for (a) STT FMR in a FM/NM bilayer and (b) SOT FMR in a single-crystalline Fe/GaAs heterostructure. j_{NM} is the microwave current flowing in NM, and j_{FM} is the microwave current in FM. h_{rf}^{NM} and h_{rf}^{FM} are the Oersted fields generated by j_{NM} and j_{FM}, respectively. In FM/NM bilayers, h_{DL} and h_{FL} are induced by j_{NM} due to the spin Hall effect and/or the inverse spin galvanic effect, while in Fe/GaAs, h_{DL} and h_{FL} are induced by j_{FM} due to the inverse spin galvanic effect.

APPENDIX A: DIFFERENCES BETWEEN STT FMR AND SOT FMR

Figures 7(a) and 7(b) present the schematics of the excitation fields for STT FMR in FM/NM bilayers and SOT FMR in single-crystalline FMs with reduced symmetry, respectively. For STT FMR, microwave current flows both in NM(j_{NM}) and FM (j_{FM}). j_{NM} induces the Oersted field h_{rf}^{NM} as well as h_{DL} and h_{FL} due to the spin Hall effect and/or the inverse spin galvanic effect. The net in-plane component of h_{rf}^{NM}, $h_{rf}^{NM,y}$, is symmetrically distributed across y, and is parallel or antiparallel to h_{FL} depending on the sign of h_{FL}, while the out of plane component of h_{rf}^{NM}, $h_{rf}^{NM,z}$, is antisymmetrically distributed across y. If the magnetization dynamics is probed by electrical measurements, $h_{rf}^{NM,z}$ contributes no net effect to the detected dc voltage. Similarly, the Oersted field h_{rf}^{FM} generated by j_{FM} is also antisymmetrically distributed, and contributes no net effect to the measured dc voltage for both SOT FMR and STT FMR. The symmetry of all the driving fields is summarized in Table I.

APPENDIX B: ELECTRICAL AND OPTICAL DETECTION OF MAGNETIZATION DYNAMICS

Figure 8(a) shows the setup for the detection of magnetization dynamics by dc voltage for STT FMR and SOT FMR. The dc voltage V_{dc} is measured by sweeping the external magnetic field at fixed microwave frequency; a typical V_{dc} trace is presented in Fig. 8(b). To fit the

TABLE I. Symmetry of the driving fields for STT FMR and SOT FMR. $h_{rf}^{NM,y}$($h_{rf}^{FM,y}$) and $h_{rf}^{NM,z}$($h_{rf}^{FM,z}$) are the in-plane and out of plane components of h_{rf}^{NM}(h_{rf}^{FM}). S^y (A^y) stands for symmetrically (antisymmetrically) distributed with respect to the y axis. A^z represents antisymmetrically distributed with respect to the z axis. For dc voltage detection of magnetization dynamics, all the antisymmetric excitations contribute no net effect to the measured dc voltage.

	h_{FL}	h_{DL}	$h_{rf}^{NM,y}$	$h_{rf}^{NM,z}$	$h_{rf}^{FM,y}$	$h_{rf}^{FM,z}$
STT FMR	S^y	S^y	S^y	A^y	A^z	A^y
SOT FMR	S^y	S^y	N.A.	N.A.	A^z	A^y
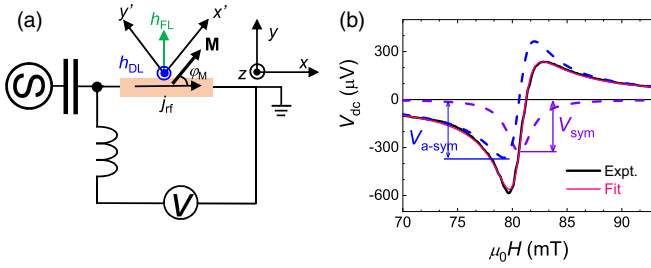
FIG. 8. (a) Depiction of a scheme for dc voltage detection of magnetization dynamics for STT FMR and SOT FMR. Here φ_M is the angle between j_{rf} and **M**. (b) Typical spectrum of the dc voltage V for STT FMR and SOT FMR around the resonance field of FM, which can be decomposed into symmetric and antisymmetric parts.

characteristic line shape, we introduce a symmetric ($L_{sym} = \Delta H^2/[4(H - H_R)^2 + \Delta H^2]$) and an antisymmetric Lorentzian ($L_{a\text{-}sym} = -4\Delta H(H - H_R)/[4(H - H_R)^2 + \Delta H^2]$). V_{dc} is fitted by a combination of L_{sym} and $L_{a\text{-}sym}$, $V_{sym}L_{sym} + V_{a\text{-}sym}L_{a\text{-}sym}$, with V_{sym} ($V_{a\text{-}sym}$) the magnitude of the symmetric (antisymmetric) component of the dc voltage. By fitting, we obtain values for H_R, ΔH, V_{sym}, and $V_{a\text{-}sym}$. H_R and ΔH are related to the magnetic properties of FM, while V_{sym} and $V_{a\text{-}sym}$ are related to the current-induced driving fields including SOFs and/or Oersted field.

Being different from V_{Kerr}, which is proportional to the real part of out of plane dynamic magnetization $\text{Re}(m_z)$, V_{dc} probes the real part of in-plane dynamic magnetization $\text{Re}(m_y)$ through the anisotropic magnetoresistance effect of FM. The total detected V_{dc} is obtained by summing up dV_{dc} for all positions of the device, i.e., $V_{dc} = \int_0^l dV_{dc}(x)$, with

$$dV_{dc}(x) = -\Delta\rho \overline{\mathbf{n}(x)[\mathbf{j}_{FM}(x) \cdot \mathbf{n}(x)]|_x} dx, \quad (B1)$$

where l is the length of the device, $\Delta\rho$ is the magnitude of the anisotropic magnetoresistance of FM, and $\mathbf{n}(x)$ is the unit dynamic magnetization at position x. In the measurement coordinate system (x, y, z), the microwave current density $\mathbf{j}_{FM}$ flows along the x direction and the dc voltage is also detected along this direction. In the coordinate system labeled (x', y', z'), $\mathbf{n}(x)$ and $\mathbf{j}_{FM}(x)$ can be respectively written as $\mathbf{n}(x) = M^{-1}(M, m_y e^{i[\omega t - \Phi_m(x)]}, m_z e^{i\omega t})$, and $\mathbf{j}_{FM}(x) = j_{FM}e^{i[\omega t - \Phi_m(x)]}(\cos\varphi_M, -\sin\varphi_M, 0)$, where m_y (m_z) is the dynamic magnetization along the y (z) direction, ω is the angular frequency of magnetization precession, and φ_M is the magnetization angle as defined in Fig. 8(a). At each position x in FM, the microwave current and the induced SOFs/Oersted field are coherently coupled (the phase difference between these two dynamic quantities is 0). Thus, $\Phi_m(x)$ cancels out, and $dV_{dc}(x)$ can be obtained as

$$dV_{dc}(x) = -\frac{\Delta\rho j_{FM}}{2M} \sin 2\varphi_M \text{Re}(m_y) dx. \quad (B2)$$

$\text{Re}(m_y)$ is obtained through the complex dynamic susceptibility as [30,38]

$$\begin{pmatrix} m_y \\ m_z \end{pmatrix} = \begin{pmatrix} \chi^i & -i\chi_a^o \\ i\chi_a^i & \chi^o \end{pmatrix} \begin{pmatrix} h^i \cos\phi_M \\ h^o \end{pmatrix}, \quad (B3)$$

where χ^i (χ_a^i) is the complex diagonal (off-diagonal) dynamic magnetic susceptibility due to the in-plane excitation h^i, and

χ^o (χ_a^o) is the complex diagonal (off-diagonal) dynamic magnetic susceptibility due to the out of plane excitation h^o. Each component of the susceptibility χ has both real and imaginary parts, $\chi = \text{Re}(\chi) + i\text{Im}(\chi)$ and can be calculated numerically. From Eq. (B3), the position dependence $\text{Re}[m_y(x)]$ can be written as

$$\text{Re}[m_y(x)] = \text{Re}(\chi^i)h^i \cos\varphi_M + \text{Im}(\chi_a^o)h^o. \quad (B4)$$

For most of the ST FMR measurements, **M** lies in plane, and h^i and h^o can be expressed as $h^i = h_{FL} + h_{rf}^{NM,y}$ and $h^o = h_{DL}$, $h_{FL}(\parallel \mathbf{y})$ and $h_{DL}(\sim \mathbf{m} \times \mathbf{y})$ represent the fieldlike and dampinglike SOFs, and $h_{rf}^{NM,y}$ the rf current-induced Oersted field in NM (for the case of SOT FMR detecting a single layer of single-crystalline FM with reduced symmetry, $h_{rf}^{NM,y} = 0$). Based on Eqs. (B2)–(B4), V_{sym} and $V_{a\text{-}sym}$ can be, respectively, expressed as

$$V_{sym} = -\frac{\Delta\rho j_{FM} l}{2M} \text{Im}(\chi_a^o) h_{DL} \sin 2\phi_M,$$

$$V_{a\text{-}sym} = -\frac{\Delta\rho j_{FM} l}{2M} \text{Re}(\chi^i)(h_{FL} + h_{rf}^{NM,y}) \cos\varphi_M. \quad (B5)$$

The magnitude of h_{DL} and $h_{FL} + h_{rf}^{NM,y}$ can be respectively determined by V_{sym} and $V_{a\text{-}sym}$ through Eq. (B5).

However, optical detection directly probes the real part of out of plane dynamic magnetization m_z, and thus the phase variation must be included in Eq. (B3) as

$$\begin{pmatrix} m_y \\ m_z \end{pmatrix} = \begin{pmatrix} \chi^i & -i\chi_a^o \\ i\chi_a^i & \chi^o \end{pmatrix} \begin{pmatrix} h^i \cos\phi_M \\ h^o \end{pmatrix} e^{i\Phi_{l-m}(x)}, \quad (B6)$$
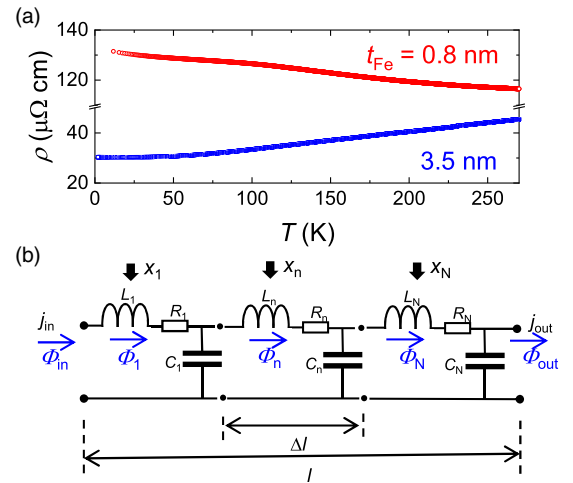
FIG. 9. (a) Temperature dependence of the resistivity of Fe/GaAs with Fe thickness t_{Fe} of 3.5 and 0.8 nm, which shows a metal-insulator transition upon decreasing t_{Fe}. (b) Equivalent transmission line circuit for $t_{Fe} = 0.8$ nm. Because the device length l is larger than the microwave guide wavelength λ_g, the transmission line can be treated as a series of N infinitesimal segments. Each segment in length Δl contains a RLC circuit, where L_n is the inductance per length, R_n the resistance per length, and C_n the capacitance. Φ_{in} is the initial phase of the input microwave current. At position x_n, the phase of the microwave current changes to Φ_n due to dielectric loss.

where $\Phi_{l-m}(x)[=\Phi_{in}+\Phi_m(x)]$ is the phase difference between the laser pulse and the dynamic magnetization at position x.

APPENDIX C: DISCUSSION OF THE MECHANISM RESPONSIBLE FOR THE VARIATION OF Φ_m

Figure 9(a) shows the temperature dependence of the resistivity for $t_{Fe}=3.5$ and 0.8 nm. One can see that the temperature coefficient changes from a metal- to a semiconductorlike behavior with decreasing t_{Fe}. This indicates that, for $t_{Fe}=0.8$ nm, the Fe film is not a good conductor anymore, but behaves like a dielectric, which can be understood from the mixing of metallic Fe and semiconducting GaAs states at the interface [39,40]. The microwave guide wavelength λ_g can be calculated by [41]

$$\lambda_g = \frac{\lambda_0}{\sqrt{\mu_r \varepsilon_r}}, \tag{C1}$$

where λ_0 is the microwave wavelength in free space, μ_r the relative permeability, and ε_r the relative permittivity. For $t_{Fe}=0.8$ nm, $\lambda_0=2.5$ cm (at 12 GHz), $\mu_r\sim1\times10^5$, $\varepsilon_r=13$ (the dielectric constant of GaAs is approximately adopted), and λ_g is estimated to be 2.5 μm, which is smaller than the length of the device l. Since $\lambda_g\ll l$, the equivalent transmission circuit can be treated as a series of N infinitesimal segments as shown in Fig. 9(b) [41]. Each segment in length Δl contains a RLC circuit, where L_n is the inductance per length, R_n the resistance per length, and C_n the capacitance to ground. Since the capacitor and inductor give a phase shift of 90°, it is expected that the phase of j_{rf}^{FM} is position dependent. This is the possible origin of position-dependent Φ_m as shown in Fig. 2(c) of the main text, and this could be similar to the case of detection of magnetization dynamics by dc voltage in a CPW, where the phase shift between inductive current and driving Oersted field may not necessarily be the same [42]. For $t_{Fe}=3.5$ nm, since the film behaves as a good metal, it is expected that j_{rf}^{FM} does not change phase along the stripe and indeed no phase variation is observed.

[1] A. Manchon, J. Železný, I. M. Miron, T. Jungwirth, J. Sinova, A. Thiaville, K. Garello, and P. Gambardella, Current-induced spin-orbit torques in ferromagnetic and antiferromagnetic systems, Rev. Mod. Phys. **91**, 035004 (2019).

[2] J. Sinova, S. O. Valenzuela, J. Wunderlich, C. H. Back, and T. Jungwirth, Spin Hall effects, Rev. Mod. Phys. **87**, 1213 (2015).

[3] I. M. Miron, K. Garello, G. Gaudin, P. Zermatten, M. V. Costache, S. Auffret, S. Bandiera, B. Rodmacq, A. Schuhl, and P. Gambadella, Perpendicular switching of a single ferromagnetic layer induced by in-plane current injection, Nature **476**, 189 (2011).

[4] L. Q. Liu, C. F. Pai, Y. Li, H. W. Tseng, D. C. Ralph, and R. A. Buhrman, Spin-torque switching with giant spin Hall effect of Tantalum, Science **336**, 555 (2012).

[5] I. M. Miron, T. Moore, H. Szambolics, L. D. Buda-Prejbeanu, S. Auffret, B. Rodmacq, S. Pizzini, J. Vogel, M. Bonfim, A. Schuhl and G. Gaudin, Fast current-induced domain-wall motion controlled by Rashba effect, Nat. Mater. **10**, 419 (2011).

[6] S. Emori, U. Bauer, S. M. Ahn, E. Martinez, and G. S. D. Beach, Current-driven dynamics of chiral ferromagnetic domain walls, Nat. Mater. **12**, 611 (2013).

[7] K. Ryu, L. Thomas, S. H. Yang, and S. Parkin, Chiral spin torque at magnetic domain walls, Nat. Nanotechnol. **8**, 527 (2013).

[8] V. E. Demidov, S. Urazhdin, H. Ulrichs, V. Tiberkevich, A. Slavin, D. Baither, G. Schmitz, and S. O. Demokritov, Magnetic nano-oscillator driven by pure spin current, Nat. Mater. **11**, 1028 (2012).

[9] L. Liu, C.-F. Pai, D. C. Ralph, and R. A. Buhrman, Magnetic Oscillations Driven by the Spin Hall Effect in 3-Terminal Magnetic Tunnel Junction Devices, Phys. Rev. Lett. **109**, 186602 (2012).

[10] L. Liu, T. Moriyama, D. C. Ralph, and R. A. Buhrman, Spin-Torque Ferromagnetic Resonance Induced by the Spin Hall Effect, Phys. Rev. Lett. **106**, 036601 (2011).

[11] C.-F. Pai, Y. Ou, L. H. Vilela-Leão, D. C. Ralph, and R. A. Buhrman, Dependence of the efficiency of spin Hall torque on the transparency of Pt/ferromagnetic layer interfaces, Phys. Rev. B **92**, 064426 (2015).

[12] Y. Ou, C.-F. Pai, S. Shi, D. C. Ralph, and R. A. Buhrman, Origin of fieldlike spin-orbit torques in heavy metal/ferromagnetic/oxide thin film heterostructures, Phys. Rev. B **94**, 140414(R) (2016).

[13] X. Fan, H. Celik, J. Wu, C. Ni, K. J. Lee, V. O. Lorenz, and J. Q. Xiao, Quantifying interface and bulk contributions to spin-orbit torque in magnetic bilayers, Nat. Commun. **5**, 3042 (2014).

[14] J. Kim, J. Sinha, M. Hayashi, M. Yamanouchi, S. Fukami, T. Suzuki, S. Mitani, and H. Ohno, Layer thickness dependence of the current-induced effective field vector in Ta|CoFeB|MgO, Nat. Mater. **12**, 240 (2013).

[15] D. Fang, H. Kurebayashi, J. Wunderlich, K. Výborný, L. P. Zârbo, R. P. Campion, A. Casiraghi, B. L. Gallagher, T. Jungwirth, and A. J. Ferguson, Spin-orbit-driven ferromagnetic resonance, Nat. Nanotechnol. **6**, 413 (2011).

[16] W. Zhang, W. Han, X. Jiang, S. H. Yang, and S. S. P. Parkin, Role of transparency of platinum-ferromagnetic interfaces in determining the intrinsic magnitude of the spin Hall effect, Nat. Phys. **11**, 496 (2015).

[17] A. R. Mellnik, J. S. Lee, A. Richardella, J. L. Grab, P. J. Mintun, M. H. Fischer, A. Vaezi, A. Manchon, E. A. Kim, N. Samarth, and D. C. Ralph, Spin-transfer torque generated by a topological insulator, Nature **511**, 449 (2014).

[18] K. Kondou, R. Yoshimi, A. Tsukazaki, Y. Fukuma, J. Matsuno, K. S. Takahashi, M. Kawasaki, Y. Tokura, and Y. Otani, Fermi-level-dependent charge-to-spin current conversion by Dirac surface states of topological insulators, Nat. Phys. **12**, 1027 (2016).

[19] Y. Wang, P. Deorani, K. Banerjee, N. Koirala, M. Brahlek, S. Oh, and H. Yang, Topological Surface States Originated Spin-Orbit Torques in Bi₂Se₃, Phys. Rev. Lett. **114**, 257202 (2015).

[20] S. Shi, S. Liang, Z. Zhu, K. Cai, S. D. Pollard, Y. Wang, J. Wang, Q. Wang, P. He, J. Yu, G. Eda, G. Liang, and H.

Yang, All-electric magnetization switching and Dzyaloshinskii-Moriya interaction in WTe$_2$/ferromagnet heterostructures, Nat. Nanotechnol. **14**, 945 (2019).

[21] H. Kurebayashi, J. Sinova, D. Fang, A. C. Irvine, T. D. Skinner, J. Wunderlich, V. Novák, R. P. Campion, B. L. Gallagher, E. K. Vehstedt, L. P. Zârbo, K. Výborný, A. J. Ferguson, and T. Jungwirth, An antidamping spin-orbit torque originating from the Berry curvature, Nat. Nanotechnol. **9**, 211 (2014).

[22] V. Tshitoyan, C. Ciccarelli, A. P. Mihai, M. Ali, M. A. C. Irvine, T. A. Moore, T. Jungwirth, and A. J. Ferguson, Electrical manipulation of ferromagnetic NiFe by antiferromagnetic IrMn, Phys. Rev. B **92**, 214406 (2015).

[23] Y. Ou, S. Shi, D. C. Ralph, and R. A. Buhrman, Strong spin Hall effect in the antiferromagnet PtMn, Phys. Rev. B **93**, 220405(R) (2016).

[24] W. Zhang, W. Han, S. H. Yang, Y. Sun, Y. Zhang, B. H. Yan, and S. S. P. Parkin, Giant facet-dependent spin-orbit torque and spin Hall conductivity in the triangular antiferromagnet IrMn$_3$, Sci. Adv. **2**, e1600759 (2016).

[25] D. MacNeill, G. M. Stiehl, M. H. D. Guimaraes, R. A. Buhrman, J. Park, and D. C. Ralph, Control of spin-orbit torques through crystal symmetry in WTe$_2$/ferromagnet bilayers, Nat. Phys. **13**, 300 (2017).

[26] M. H. D. Guimarães, G. M. Stiehl, D. MacNeill, N. D. Reynolds, and D. C. Ralph, Spin-orbit torques in NbSe$_2$/permalloy bilayers, Nano. Lett. **18**, 1311 (2018).

[27] S. Husain, X. Chen, R. Gupta, N. Behera, P. Kumar, T. Edvinsson, F. García-Sánchez, R. Brucas, S. Chaudhary, B. Sanyal, P. Svedlindh, and A. Kumar, Large damping-like spin-orbit torque in 2D conductive 1T-TaS monolayer, Nano Lett. **20**, 6372 (2020).

[28] G. M. Stiehl, D. MacNeill, N. Sivadas, I. E. Baggari, M. H. D. Guimarães, N. D. Reynolds, L. F. Kourkoutis, C. J. Fennie, R. A. Buhrman, and D. C. Ralph, Current-induced torques with Dresselhaus symmetry due to resistance anisotropy in 2D materials, ACS Nano **13**, 2599 (2019).

[29] F. Guo, J. M. Bartell, and G. D. Fuchs, Ferromagnetic resonance phase imaging in spin Hall multilayers, Phys. Rev. B **93**, 144415 (2016).

[30] L. Chen, M. Decker, M. Kronseder, R. Islinger, M. Gmitra, D. Schuh, D. Bougeard, J. Fabian, and C. H. Back, Robust spin-orbit torque and spin-galvanic effect at the Fe/GaAs (001) interface at room temperature, Nat. Commun. **7**, 13802 (2016).

[31] J. Stigloher, M. Decker, H. S. Körner, K. Tanabe, T. Moriyama, T. Taniguchi, H. Hata, M. Madami, G. Gubbiotti, K. Kobayashi, T. Ono, and C. H. Back, Snell's Law for Spin Wave, Phys. Rev. Lett. **117**, 037204 (2016).

[32] See Supplemental Material at http://link.aps.org/supplemental/10.1103/PhysRevB.104.014425 for samples, devices, TRMOKE measurements, the phase shift in Py/Bi$_2$Se$_3$ bilayers, the details for micromagnetic simulations, the fitting procedure of SSW imaging, the comparison of the SOFs obtained by SOT-FMR and SSW imaging, and the proposal for the determination of SOFs in FM/HM bilayers. References [13,30,33] are also included here.

[33] A. Vansteenkiste, J. Leliaert, M. Dvornik, F. Garcia-Sanchez, and B. Van Waeyenberge, The design and verification of MU-MAX3, AIP Adv. **4**, 107133 (2014).

[34] Y. Kajiwara, K. Harii, S. Takahashi, J. Ohe, K. Uchida, M. Mizuguchi, H. Umezawa, H. Kawai, K. Ando, K. Takanashi, S. Maekawa, and E. Saitoh, Transmission of electrical signals by spin-wave interconversion in a magnetic insulator, Nature **464**, 262 (2010).

[35] C. Bayer, J. Jorzick, B. Hillebrands, S. O. Demokritov, R. Kouba, R. Bozinoski, A. N. Slavin, K. Y. Guslienko, D. V. Berkov, N. L. Gorn, and M. P. Kostylev, Spin-wave excitations in finite rectangular element of Ni$_{80}$Fe$_{20}$, Phys. Rev. B **72**, 064427 (2005).

[36] *Spin Dynamics in Confined Magnetic Structures III*, edited by B. Hillebrands and A. Thiaville (Springer, Berlin, 2006).

[37] M. A. W. Schoen, D. Thonig, M. L. Schneider, T. J. Silva, H. T. Nembach, O. Eriksson, O. Karis, and J. M. Shaw, Ultra-low magnetic damping of a metallic ferromagnet, Nat. Phys. **12**, 839 (2016).

[38] L. Chen, F. Matsukura, and H. Ohno, Direct-current volatges in (Ga,Mn)As structures induced by ferromagnetic resonance, Nat. Commun. **4**, 2055 (2013).

[39] M. Gmitra, A. Matos-Abiague, C. Draxl, and J. Fabian, Magnetic Control of Spin-Orbit Fields, Phys. Rev. Lett. **111**, 036603 (2013).

[40] T. Hupfauer, A. Matos-Abiague, M. Gmitra, F. Schiller, J. Loher, D. Bougeard, C. H. Back, J. Fabian, and D. Weiss, Emergence of spin-orbit fields in magnetotransport of quasi-two-dimensional iron on gallium arsenide, Nat. Commun. **6**, 7374 (2015).

[41] B. C. Wadell, *Transmission Line Design Handbook* (Artech House, Inc., Norwood, MA, 1991).

[42] M. Harder, Z. X. Cao, Y. S. Gui, X. L. Fan, and C. M. Hu, Analysis of the line shape of electrically detected ferromagnetic resonance, Phys. Rev. B **84**, 054423 (2011).